

Towards human SuperEEG

Lucy L. W. Owen¹, Andrew C. Heusser^{1,2}, and Jeremy R. Manning^{1*}

¹Department of Psychological and Brain Sciences, Dartmouth College,
Hanover, NH 03755, USA

²Akili Interactive,
Boston, MA 02110, USA

Abstract

Human *SuperEEG*¹ entails measuring ongoing neural activity with perfect precision and at arbitrarily high spatiotemporal resolution. Although true SuperEEG is impossible using existing methods, here we present a model-based method for *inferring* neural activity at millimeter-scale spatial resolutions and millisecond-scale temporal resolutions using standard human intracranial recordings. Our approach assumes that different people's brains exhibit similar spatial correlations, and that (all else being equal) neural activity at nearby locations will tend to be similar. One can then ask, for an arbitrary individual's brain: given recordings from a limited set of locations in that individual's brain, along with the observed spatial correlations learned from other people's recordings, how much can be inferred about ongoing activity at *other* locations in that individual's brain?

Keywords: Electrocorticography (ECoG), intracranial electroencephalography (iEEG), local field potential (LFP), epilepsy, maximum likelihood estimation, Gaussian process regression

Introduction

Modern human brain recording techniques are fraught with compromise [?]. Commonly used approaches include functional magnetic resonance imaging (fMRI), scalp electroencephalography (EEG), and magnetoencephalography (MEG). For each of these techniques, neuroscientists and electrophysiologists must choose to optimize spatial resolution at the cost of temporal resolution (e.g., as in fMRI) or temporal resolution at the cost of spatial resolution (e.g., as in EEG and MEG). A less widely used approach (due to requiring work with neurosurgical patients) is to record from electrodes implanted directly onto the cortical surface (electrocorticography; ECoG)

¹The term "SuperEEG" was coined by Robert J. Sawyer in his popular science fiction novel *The Terminal Experiment* [?]

25 or into deep brain structures (intracranial EEG; iEEG). However, these intracranial approaches
26 also require compromise: the high spatiotemporal resolutions of intracranial recordings comes
27 at the cost of substantially reduced brain coverage, since safety considerations limit the number
28 of electrodes one may implant in a given patient's brain. Further, the locations of implanted
29 electrodes are determined by clinical, rather than research, needs.

30 An increasingly popular approach is to improve the effective spatial resolution of MEG or
31 scalp EEG data by using a geometric approach called *beamforming* to solve the biomagnetic or
32 bioelectrical inverse problem [?]. This approach entails using detailed brain conductance mod-
33 els (often informed by high spatial resolution anatomical MRI images) along with the known
34 sensor placements (localized precisely in 3D space) to reconstruct brain signals originating from
35 theoretical point sources deep in the brain (and far from the sensors). Traditional beamforming
36 approaches must overcome two obstacles. First, the inverse problem beamforming seeks to
37 solve has infinitely many solutions. Researchers have made traction towards constraining the
38 solution space by assuming that signal-generating sources are localized on a regularly spaced
39 grid spanning the brain and that individual sources are small relative to their distances to the
40 sensors [? ? ?]. The second, and in some ways much more serious, obstacle is that the
41 magnetic fields produced by external (noise) sources are substantially stronger than those pro-
42 duced by the neuronal changes being sought (i.e., at deep structures, as measured by sensors
43 at the scalp). This means that obtaining adequate signal quality often requires averaging the
44 measured responses over tens to hundreds of responses or trials (e.g., see review by [?]).

45 Another approach to obtaining high spatiotemporal resolution neural data has been to col-
46 lect fMRI and EEG data simultaneously. Simultaneous fMRI-EEG has the potential to balance
47 the high spatial resolution of fMRI with the high temporal resolution of scalp EEG, thereby,
48 in theory, providing the best of both worlds. In practice, however, the signal quality of both
49 recordings suffers substantially when the two techniques are applied simultaneously (e.g., see

50 review by [?]). In addition, the experimental designs that are ideally suited to each technique
51 individually are somewhat at odds. For example, fMRI experiments often lock stimulus presen-
52 tation events to the regularly spaced image acquisition time (TR), which maximizes the number
53 of post-stimulus samples. By contrast, EEG experiments typically employ jittered stimulus pre-
54 sentation times to maximize the experimentalist’s ability to distinguish electrical brain activity
55 from external noise sources such as from 60 Hz alternating current power sources.

56 The current “gold standard” for precisely localizing signals and sampling at high temporal
57 resolution is to take (ECoG or iEEG) recordings from implanted electrodes (but from a limited
58 set of locations in any given brain). This begs the following question: what can we infer about the
59 activity exhibited by the rest of a person’s brain, given what we learn from the limited intracranial
60 recordings we have from their brain and additional recordings taken from *other* people’s brains?

61 Here we develop an approach, which we call *SuperEEG*, based on Gaussian process regression [?
62]. SuperEEG entails using data from multiple people to estimate activity patterns at arbitrary
63 locations in each person’s brain (i.e., independent of their electrode placements). We test
64 SuperEEG approach using two large datasets of intracranial recordings [? ? ? ? ? ? ? ? ? ? ? ? ? ? ? ? ? ?].
65 We show that the SuperEEG algorithm recovers signals well from electrodes that were held
66 out of the training dataset. We also examine the factors that influence how accurately activity
67 may be estimated (recovered), which may have important implications for electrode design and
68 placement in neurosurgical applications.

69 Approach

70 The SuperEEG approach to inferring high temporal resolution full-brain activity patterns is
71 outlined and summarized in Figure 1. We describe (in this section) and evaluate (in *Results*) our
72 approach using a two large previously collected dataset comprising multi-session intracranial
73 recordings. Dataset 1 comprises multi-session recordings taken from 6876 electrodes implanted

74 in the brains of 88 epilepsy patients [? ? ? ? ?]. Each recording session lasted from 0.2–3.0
75 (total recording time: 0.3–14.2 hours; Fig. S4A), and includes data from a list-learning memory
76 experiment for up to one hour varying by patient with additional buffer time in which the
77 patients performed typical bed-ridden hospital activities. For the purposes of the Dataset
78 1 analyses presented here, we aggregated all data across each recording session, ignoring the
79 particular activities or tasks the patients were performing at any given moment. We used Dataset
80 1 to develop our main SuperEEG approach, and to examine the extent to which SuperEEG might
81 be able to generate task-general predictions. Dataset 2 comprised multi-session recordings from
82 4436 electrodes implanted in the brains of 40 epilepsy patients [? ? ? ? ? ? ? ? ?]. Each
83 recording session lasted from 0.4–2.2 hours (total recording time: 0.4–6.6 hours; Fig. S4B).
84 Whereas Dataset 1 included recordings taken during a wide variety of behaviors, Dataset 2
85 included recordings taken as each patient performed each of two memory tasks: a random
86 word list free recall task and a categorized word list free recall task. We used Dataset 2 to
87 further examine the ability of SuperEEG to generalize its predictions within versus across tasks.
88 Figure S4 provides additional details on both datasets.

89 We first applied fourth order Butterworth notch filter to remove 60 Hz ($\pm .5$ Hz) line noise
90 from every recording (from every electrode). Next, we downsampled the recordings (regardless
91 of the original samplerate) to 250 Hz. (This downsampling step served to both normalize for
92 differences in sampling rates across patients and to ease the computational burden of our
93 subsequent analyses.) We then excluded any electrodes that showed putative epileptiform
94 activity. Specifically, we excluded from further analysis any electrode that exhibited an average
95 kurtosis of 10 or greater across all of that patient's recording sessions. We also excluded any
96 patients with fewer than 2 electrodes that passed this criteria, as the SuperEEG algorithm
97 requires measuring correlations between 2 or more electrodes from each patient. For Dataset
98 1, this yielded clean recordings from 4168 electrodes implanted throughout the brains of 67

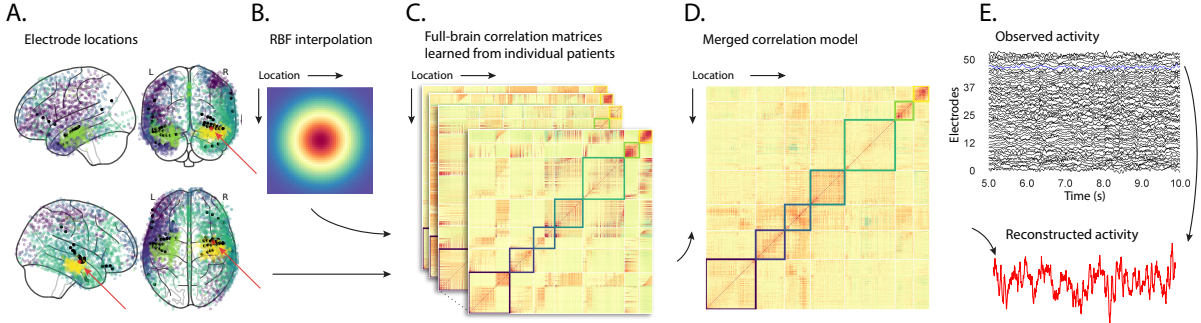


Figure 1: Methods overview. **A. Electrode locations.** Each dot reflects the location of a single electrode implanted in the brain of a Dataset 1 patient. A held-out recording location from one patient is indicated in red, and the patient’s remaining electrodes are indicated in black. The electrodes from the remaining patients are colored by k -means cluster (computed using the full-brain correlation model shown in Panel D). **B. Radial basis function kernel.** Each electrode contributed by the patient (black) weights on the full set of locations under consideration (all dots in Panel A, defined as \bar{R} in the text). The weights fall off with positional distance (in MNI space) according to an RBF. **C. Per-patient correlation matrices.** After computing the pairwise correlations between the recordings from each patient’s electrodes, we use RBF-weighted averages to estimate correlations between all locations in \bar{R} . We obtain an estimated full-brain correlation matrix using each patient’s data. **D. Merged correlation model.** We combine the per-patient correlation matrices (Panel C) to obtain a single full-brain correlation model that captures information contributed by every patient. Here we have sorted the rows and columns to reflect k -means clustering labels [using $k=7$; ?], whereby we grouped locations based on their correlations with the rest of the brain (i.e., rows of the matrix displayed in the panel). The boundaries denote the cluster groups. The rows and columns of Panel C have been sorted using the Panel D-derived cluster labels. **E. Reconstructing activity throughout the brain.** Given the observed recordings from the given patient (shown in black; held-out recording is shown in blue), along with a full-brain correlation model (Panel D), we use Equation 12 to reconstruct the most probable activity at the held-out location (red).

⁹⁹ patients (Fig. 1A); for Dataset 2, this yielded clean recordings from 3159 electrodes from 24
¹⁰⁰ patients. Each individual patient contributes electrodes from a limited set of brain locations,
¹⁰¹ which we localized in a common space [MNI152; ?]; an example Dataset 1 patient’s 54 electrodes
¹⁰² that passed the predefined kurtosis test are highlighted in black and red.

The recording from a given electrode is maximally informative about the activity of the neural tissue immediately surrounding its recording surface. However, brain regions that are distant from the recording surface of the electrode also contribute to the recording, albeit (*ceteris paribus*) to a much lesser extent. One mechanism underlying these contributions is volume conduction. The precise rate of falloff due to volume conduction (i.e., how much a small volume of brain tissue at location x contributes to the recording from an electrode at location η) depends on the size of the recording surface, the electrode’s impedance, and the conductance profile of the volume of brain between x and η . As an approximation of this intuition, we place a Gaussian radial basis function (RBF) at the location η of each electrode’s recording surface (Fig. 1B). We use the values of the RBF at any brain location x as a rough estimate of how much structures around x contributed to the recording from location η :

$$\text{rbf}(x|\eta, \lambda) = \exp \left\{ -\frac{\|x - \eta\|^2}{\lambda} \right\}, \quad (1)$$

¹⁰³ where the width variable λ is a parameter of the algorithm (which may in principle be set
¹⁰⁴ according to location-specific tissue conductance profiles) that governs the level of spatial
¹⁰⁵ smoothing. In choosing λ for the analyses presented here, we sought to maximize spatial
¹⁰⁶ resolution (which implies a small value of λ) while also maximizing the algorithm’s ability
¹⁰⁷ to generalize to any location throughout the brain, including those without dense electrode
¹⁰⁸ coverage (which implies a large value of λ). Here we set $\lambda = 20$, guided in part by our prior
¹⁰⁹ work [? ?], and in part by examining the brain coverage with non-zero weights achieved by
¹¹⁰ placing RBFs at each electrode location in Dataset 1 and taking the sum (across all electrodes)
¹¹¹ at each voxel in a 4 mm^3 MNI brain. (We then held λ fixed for our analyses of Dataset 2.) We

¹¹² note that this value could in theory be further optimized, e.g., using cross validation or a formal
¹¹³ model [e.g., ?].

¹¹⁴ A second mechanism whereby a given region x can contribute to the recording at η is
¹¹⁵ through (direct or indirect) anatomical connections between structures near x and η . We use
¹¹⁶ temporal correlations in the data to estimate these anatomical connections [?]. Let \bar{R} be the
¹¹⁷ set of locations at which we wish to estimate local field potentials, and let $R_s \subseteq \bar{R}$ be set of
¹¹⁸ locations at which we observe local field potentials from patient s (excluding the electrodes that
¹¹⁹ did not pass the kurtosis test described above). In the analyses below we define $\bar{R} = \cup_{s=1}^S R_s$.
¹²⁰ We can calculate the expected inter-electrode correlation matrix for patient s , where $C_{s,k}(i, j)$ is
¹²¹ the correlation between the time series of voltages for electrodes i and j from subject s during
¹²² session k , using:

$$\bar{C}_s = r\left(\frac{1}{n}\left(\sum_{k=1}^n z(C_{s,k})\right)\right), \text{ where} \quad (2)$$

$$z(r) = \frac{\log(1+r) - \log(1-r)}{2} \text{ is the Fisher } z\text{-transformation and} \quad (3)$$

$$z^{-1}(z) = r(z) = \frac{\exp(2z) - 1}{\exp(2z) + 1} \text{ is its inverse.} \quad (4)$$

¹²³ Next, we use Equation 1 to construct a number of to-be-estimated locations by number of
¹²⁴ patient electrode locations weight matrix, W_s . Specifically, W_s approximates how informative
¹²⁵ the recordings at each location in R_s are in reconstructing activity at each location in \bar{R} , where
¹²⁶ the contributions fall off with an RBF according to the distances between the corresponding
¹²⁷ locations:

$$W_s(i, j) = \text{rbf}(i|j, \lambda). \quad (5)$$

¹²⁸ Given this weight matrix, W_s , and the observed inter-electrode correlation matrix for patient
¹²⁹ s , \bar{C}_s , we can estimate the correlation matrix for all locations in \bar{R} (\hat{C}_s ; Fig. 1C) using:

$$\hat{N}_s(x, y) = \sum_{i=1}^{|R_s|} \sum_{j=1}^{i-1} W(x, i) \cdot W(y, j) \cdot z(\bar{C}_s(i, j)) \quad (6)$$

$$\hat{D}_s(x, y) = \sum_{i=1}^{|R_s|} \sum_{j=1}^{i-1} W(x, i) \cdot W(y, j). \quad (7)$$

$$\hat{C}_s = r \left(\frac{\hat{N}_s}{\hat{D}_s} \right). \quad (8)$$

After estimating the numerator (\hat{N}_s) and denominator (\hat{D}_s) placeholders for each \hat{C}_s , we aggregate these estimates across the S patients to obtain a single expected full-brain correlation matrix (\hat{K} ; Fig. 1D):

$$\hat{K} = r \left(\frac{\sum_{s=1}^S \hat{N}_s}{\sum_{s=1}^S \hat{D}_s} \right). \quad (9)$$

Intuitively, the numerators capture the general structures of the patient-specific estimates of full-brain correlations, and the denominators account for which locations were near the implanted electrodes in each patient. To obtain \hat{K} , we compute a weighted average across the estimated patient-specific full-brain correlation matrices, where patients with observed electrodes near a particular set of locations in \hat{K} contribute more to the estimate.

Having used the multi-patient data to estimate a full-brain correlation matrix at the set of locations in \bar{R} that we wish to know about, we next use \hat{K} to estimate activity patterns everywhere in \bar{R} , given observations at only a subset of locations in \bar{R} (Fig. 1E).

Let α_s be the set of indices of patient s 's electrode locations in \bar{R} (i.e., the locations in R_s), and let β_s be the set of indices of all other locations in \bar{R} . In other words, β_s reflects the locations in \bar{R} where we did not observe a recording for patient s (these are the recording locations we will want to fill in using SuperEEG). We can sub-divide \hat{K} as follows:

$$\hat{K}_{\beta_s, \alpha_s} = \hat{K}(\beta_s, \alpha_s), \text{ and} \quad (10)$$

$$\hat{K}_{\alpha_s, \alpha_s} = \hat{K}(\alpha_s, \alpha_s). \quad (11)$$

142 Here $\hat{K}_{\beta_s, \alpha_s}$ represents the correlations between the “unknown” activity at the locations in β_s
 143 and the observed activity at the locations in α_s , and $\hat{K}_{\alpha_s, \alpha_s}$ represents the correlations between
 144 the observed recordings (at the locations in α_s).

145 Let Y_{s,k,α_s} be the number-of-timepoints (T) by $|\alpha_s|$ matrix of (observed) voltages from the
 146 electrodes in α_s during session k from patient s . Then we can estimate the voltage from patient
 147 s ’s k^{th} session at the locations in β_s using [?]:

$$\hat{Y}_{s,k,\beta_s} = ((\hat{K}_{\beta_s, \alpha_s} \cdot \hat{K}_{\alpha_s, \alpha_s}^{-1}) \cdot Y_{s,k,\alpha_s}^T)^T. \quad (12)$$

148 This equation is the foundation of the SuperEEG algorithm. Whereas we observe recordings
 149 only at the locations indexed by α_s , Equation 12 allows us to estimate the recordings at all loca-
 150 tions indexed by β_s , which we can define *a priori* to include any locations we wish, throughout
 151 the brain. This yields estimates of the time-varying voltages at *every* location in \bar{R} , provided that
 152 we define \bar{R} in advance to include the union of all of the locations in R_s and all of the locations
 153 at which we wish to estimate recordings (i.e., a timeseries of voltages).

154 We designed our approach to be agnostic to electrode impedances, as electrodes that do not
 155 exist do not have impedances. Therefore our algorithm recovers voltages in standard deviation
 156 (z -scored) units rather than attempting to recover absolute voltages. (This property reflects
 157 the fact that $\hat{K}_{\beta_s, \alpha_s}$ and $\hat{K}_{\alpha_s, \alpha_s}$ are correlation matrices rather than covariance matrices.) Also,
 158 note that Equation 12 requires computing a T by T matrix, which can become computationally
 159 intractable when T is very large (e.g., for the patient highlighted in Fig. 2, $T = 12786750$).

¹⁶⁰ However, because Equation 12 is time invariant, we may compute Y_{s,k,β_s} in a piecewise manner
¹⁶¹ by filling in Y_{s,k,β_s} one row at a time (using the corresponding samples from Y_{s,k,α_s}).

¹⁶² The SuperEEG algorithm described above and in Figure 1 allows us to estimate, up to a
¹⁶³ constant scaling factor, local field potentials (LFPs) for each patient at all arbitrarily chosen
¹⁶⁴ locations in the set \bar{R} , even if we did not record that patient's brain at all of those locations. We next
¹⁶⁵ turn to an evaluation of the accuracy of those estimates.

¹⁶⁶ Results

¹⁶⁷ We used a cross-validation approach to test the accuracy with which the SuperEEG algorithm
¹⁶⁸ reconstructs activity throughout the brain. For each patient in turn, we estimated full-brain
¹⁶⁹ correlation matrices (Eqn. 9) using data from all of the *other* patients. This step ensured that the
¹⁷⁰ data we were reconstructing could not also be used to estimate the between-location correlations
¹⁷¹ that drove the reconstructions via Equation 12 (otherwise the analysis would be circular). For
¹⁷² that held-out patient, for each of their electrodes in turn, we used Equation 12 to reconstruct
¹⁷³ activity at the held-out electrode location, using the correlation matrix learned from all other
¹⁷⁴ patients' data as \hat{K} , and using activity recorded from the other electrodes from the held-out
¹⁷⁵ patient as Y_{s,k,α_s} . We then asked: how closely did each of the SuperEEG-estimated recordings
¹⁷⁶ at those electrodes match the observed recordings from those electrodes (i.e., how closely did
¹⁷⁷ the estimated \hat{Y}_{s,k,β_s} match the observed Y_{s,k,β_s} ?).

¹⁷⁸ To illustrate our approach, we first examine an individual held-out raw LFP trace and its
¹⁷⁹ associated SuperEEG-derived reconstruction. Figure 2A displays the observed LFP from the red
¹⁸⁰ electrode in Figure 1A (blue), and its associated reconstruction (red), during a 5 s time window
¹⁸¹ during one of the example patient's six recording sessions. The two traces match closely
¹⁸² ($r = 0.86, p < 10^{-10}$). Figure 2B displays a two-dimensional histogram of the actual versus
¹⁸³ reconstructed voltages for the entire 14.2 total hours of recordings from the example electrode

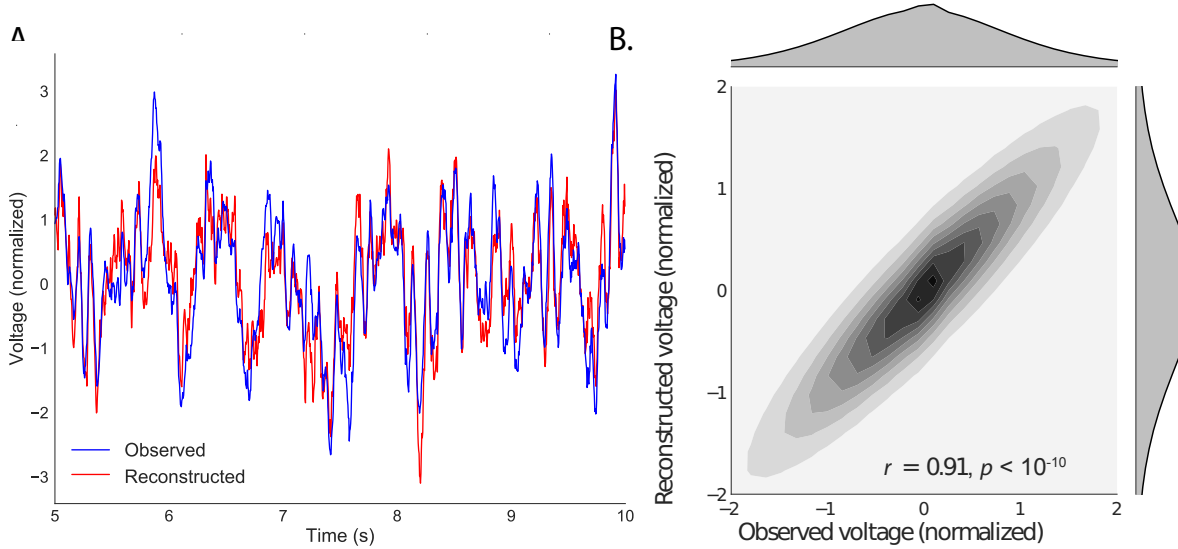


Figure 2: Observed and reconstructed LFP from a single electrode. **A. Example LFP.** A 5 s recording from the red electrode in Figure 1A is displayed in blue, and the reconstructed LFP during the same time window is shown in red. **B. Observed versus reconstructed LFP over 14.2 hours.** The two-dimensional histogram reflects the relation between distributions of observed versus reconstructed voltages from one patient, across the 14.2 hours of recorded data collected over 6 recording sessions. The correlation reported in the panel is between the observed and reconstructed voltages. Both panels: all voltages are represented in standard deviation units (computed within session).

(correlation: $r = 0.91, p < 10^{-10}$). This example confirms that the SuperEEG algorithm recovers the recordings from this single electrode well. Next, we used this general approach to quantify the algorithm's performance across the full dataset.

For each held-out electrode, from each held-out patient in turn, we computed the average correlation (across recording sessions) between the SuperEEG-reconstructed voltage traces and the observed voltage traces from that electrode. For this analysis we set \bar{R} to be the union of all electrode locations across all patients. This yielded a single correlation coefficient for each electrode location in \bar{R} , reflecting how well the SuperEEG algorithm was able to recover the recording at that location by incorporating data across patients (black histogram in Fig. 3A, map in Fig. 3C). The observed distribution of correlations was centered well above zero (mean: 0.52;

¹⁹⁴ t -test comparing mean of distribution of z -transformed average patient correlation coefficients
¹⁹⁵ to 0: $t(66) = 25.08, p < 10^{-10}$), indicating that the SuperEEG algorithm recovers held-out
¹⁹⁶ activity patterns substantially better than random guessing.

¹⁹⁷ As a stricter benchmark, we compared the quality of these across-participant reconstructions
¹⁹⁸ (i.e., computed using a correlation model learned from other patients' data) to reconstructions
¹⁹⁹ generated using a correlation model trained using the in-patient's data. In other words, for
²⁰⁰ this within-patient benchmark analysis we estimated \hat{C}_s (Eqn. 8) for each patient in turn, using
²⁰¹ recordings from all of that patient's electrodes except at the location we were reconstructing.
²⁰² These within-patient reconstructions serve as an estimate of how well data from all of the
²⁰³ other electrodes from that single patient may be used to estimate held-out data from the
²⁰⁴ same patient. This allows us to ask how much information about the activity at a given
²⁰⁵ electrode might be inferred through (a) volume conductance or other sources of "leakage"
²⁰⁶ from activity patterns measured from the patient's other electrodes and (b) across-electrode
²⁰⁷ correlations learned from that single patient. As shown in Figure 3A (gray histogram), the
²⁰⁸ distribution of within-patient correlations was centered well above zero (mean: 0.32; t -test
²⁰⁹ comparing mean of distribution of z -transformed average patient correlation coefficients to 0:
²¹⁰ $t(66) = 15.16, p < 10^{-10}$). However, the across-patient correlations were substantially higher
²¹¹ (t -test comparing average z -transformed within versus across patient electrode correlations:
²¹² $t(66) = 9.62, p < 10^{-10}$). This is an especially conservative test, given that the across-patient
²¹³ SuperEEG reconstructions exclude (from the correlation matrix estimates) all data from the
²¹⁴ patient whose data is being reconstructed. We repeated each of these analyses on a second
²¹⁵ independent dataset and found similar results (Fig. 3B, D; within versus across reconstruction
²¹⁶ accuracy: $t(23) = 6.93, p < 10^{-5}$). We also replicated this result separately for each of the two
²¹⁷ experiments from Dataset 2 (Fig. S1). This overall finding, that reconstructions of held-out
²¹⁸ data using correlation models learned from *other* patient's data yield higher reconstruction

accuracy than correlation models learned from the patient whose data is being reconstructed, has two important implications. First, it implies that distant electrodes provide additional predictive power to the data reconstructions beyond the information contained solely in nearby electrodes. (This follows from the fact that each patient’s electrodes are implanted in a unique set of locations, so for any given electrode the closest electrodes in the full dataset are likely to come from the same patient.) Second, it implies that the spatial correlations learned using the SuperEEG algorithm are, to some extent, similar across people.

The recordings we analyzed from Dataset 1 comprised data collected as the patients performed a variety of (largely idiosyncratic) tasks throughout each day’s recording session. That we observed reliable reconstruction accuracy across patients suggests that the spatial correlations derived from the SuperEEG algorithm are, to some extent, similar across tasks. We tested this finding more explicitly using Dataset 2. In Dataset 2, the recordings were limited to times when each patient was participating in each of two experiments (Experiment 1, a random-word list free recall task, and Experiment 2, a categorized list free recall task). We wondered whether a correlation model learned from data from one experiment might yield good predictions of data from the other experiment. Further, we wondered about the extent to which it might be beneficial or harmful to combine data across tasks.

To test the task-specificity of the SuperEEG-derived correlation models, we repeated the above within- and across-patient cross validation procedures separately for Experiment 1 and Experiment 2 data from Dataset 2. We then compared the reconstruction accuracies for held-out electrodes, for models trained within versus across the two experiments, or combining across both experiments (Fig. S2). In every case we found that across-patient models trained using data from all other patients out-performed within-patient models trained on data only from the subject contributing the given electrode ($ts(24) > 6.50, ps < 10^{-5}$). All reconstruction accuracies also reliably exceeded chance performance ($ts(24) > 8.00, ps < 10^{-8}$). Average reconstruction

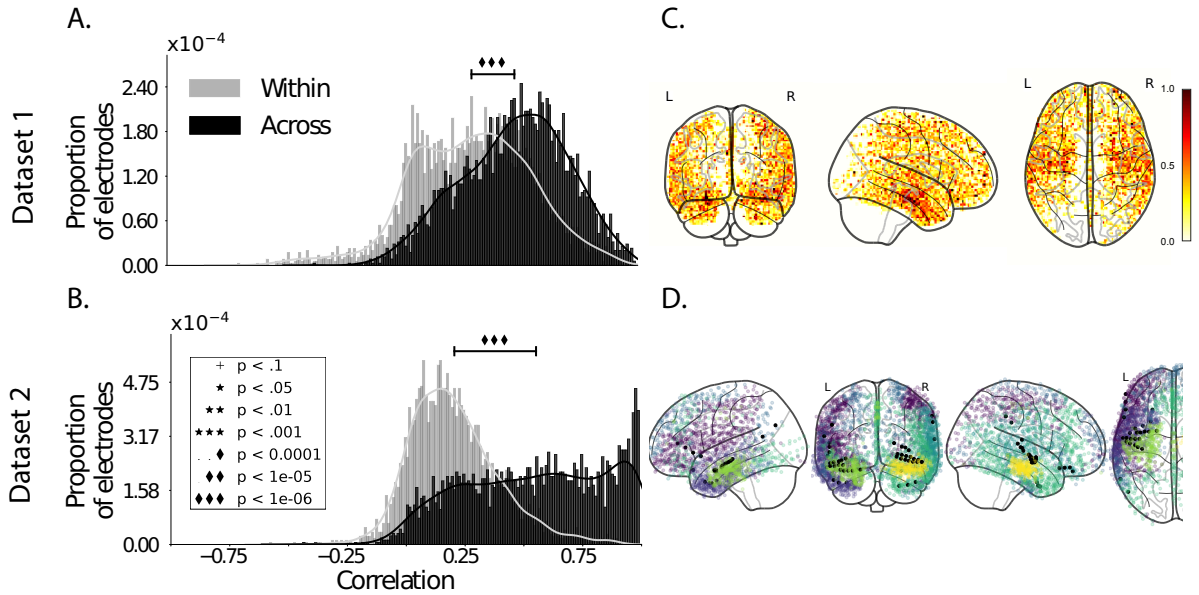


Figure 3: Reconstruction quality across all electrodes in two ECoG datasets. A. Distributions of correlations between observed versus reconstructed activity by electrode, for Dataset 1. The across-patient distribution (black) reflects reconstruction accuracy (correlation) using a correlation model learned from all but one patient's data, and then applied to that held-out patient's data. The within-patient distribution (gray) reflects performance using a correlation model learned from the same patient who contributed the to-be-reconstructed electrode. **B. Distributions of correlations for Dataset 2.** This panel is in the same format as Panel A, but reflects results obtained from Dataset 2. The histograms aggregate data across both Dataset 2 experiments; for results broken down by experiment see Figure S3. **C.–D. Reconstruction performance by location.** Each dot reflects the location of a single implanted electrode from Dataset 1 (Panel C) or Dataset 2 (Panel D). The dot colors denote the average across-session correlation, using the across-patient correlation model, between the observed and reconstructed activity at the given electrode location.

accuracy was highest for the across-patient models limited to data from the same experiment (mean accuracy: 0.68); next-highest for the across-patient models that combined data across both experiments (mean accuracy: 0.61); and lowest for models trained across task (mean accuracy: 0.47). This result also held for each of the Dataset 2 experiments individually (Fig. S3). Taken together, these results indicate that there are reliable commonalities in the spatial correlations of full-brain activity across tasks, but that there are also reliable differences in these spatial correlations across tasks. Whereas reconstruction accuracy benefits from incorporating data from other patients, reconstruction accuracy is highest when constrained to within-task data, or data that includes a variety of tasks (e.g., Dataset 1, or combining across the two Dataset 2 experiments).

Although both datasets we examined provide good full-brain coverage (when considering data from every patient; e.g. Fig. 3C, D), electrodes are not placed uniformly throughout the brain. For example, electrodes are more likely to be implanted in regions like the medial temporal lobe (MTL), and are rarely implanted in occipital cortex (Fig. 4A, B). Separately for each dataset, for each voxel in the 4 mm^3 voxel MNI152 brain, we computed the proportion of electrodes in the dataset that were contained within a 20 MNI unit radius sphere centered on that voxel. We defined the *density* at that location as this proportion. Across Datasets 1 and 2, the electrode placement densities were similar (correlation by voxel: $r = 0.56, p < 10^{-10}$). We wondered whether regions with good coverage might be associated with better reconstruction accuracy (e.g. Fig. 3C, D indicate that many electrodes in the MTL have relatively high reconstruction accuracy, and occipital electrodes tend to have relatively low reconstruction accuracy). To test whether this held more generally across the entire brain, for each dataset we computed the electrode placement density for each electrode from each patient (using the proportion of *other* patients' electrodes within 20 MNI units of the given electrode). We then correlated these density values with the across-patient reconstruction accuracies for each

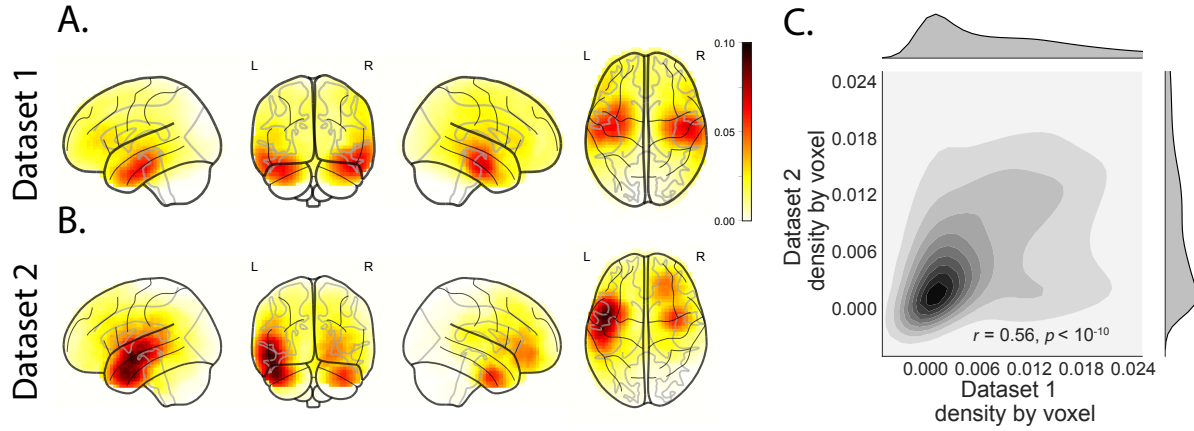


Figure 4: Electrode sampling density by location. **A. Electrode sampling density by voxel in Dataset 1.** Each voxel is colored by the proportion of total electrodes in the dataset that are located within a 20 MNI unit radius sphere centered on the given voxel. **B. Electrode sampling density by voxel in Dataset 2.** This panel displays the sampling density map for Dataset 2, in the same format as Panel A. **C. Correspondence in sampling density by voxel across Datasets 1 and 2.** The two-dimensional histogram displays the by-voxel densities in the two Datasets, and the one-dimensional histograms display the proportions of voxels in each dataset with the given density value. The correlation reported in the panel is across voxels in the 4 mm^3 MNI brain.

269 electrode. Contrary to our expectation, rather than positive correlations, we found weak (but
 270 reliable) negative correlations between reconstruction accuracy and density for both datasets
 271 (Dataset 1: $r = -0.07, p < 10^{-5}$; Dataset 2: $r = -0.18, p < 10^{-10}$). This indicates that the
 272 reconstruction accuracies we observed are not driven solely by sampling density, but rather
 273 may also reflect higher order properties of neural dynamics such as functional correlations
 274 between distant voxels [?].

275 In neurosurgical applications where one wishes to infer full-brain activity patterns, can our
 276 framework yield insights into where the electrodes should be placed? A basic assumption of our
 277 approach (and of most prior ECoG work) is that electrode recordings are most informative about
 278 the neural activity near the recording surface of the electrode. But if we consider that activity
 279 patterns throughout the brain are meaningfully correlated, are there particular implantation
 280 locations that, if present in a patient's brain, yield especially high reconstruction accuracies

throughout the rest of the brain? For example, one might hypothesize that brain structures that are heavily interconnected with many other structures could be more informative about full-brain activity patterns than comparatively isolated structures.

To gain insights into whether particular electrode locations might be especially informative, we first computed the average reconstruction accuracy across all of each patient's electrodes (using the across-patients cross validation test; black histograms in Fig. 3A and B). We labeled each patient's electrodes in each dataset with the average reconstruction accuracy for that patient. In other words, we assigned every electrode from each given patient the same value, reflecting how well the activity patterns at those electrodes were reconstructed on average. Next, for each voxel in the 4 mm³ MNI brain, we computed the average value across any electrode (from any patient) that came within 20 MNI units of that voxel's center. Effectively, we computed an *information score* for each voxel, reflecting the average reconstruction accuracy across any patients with electrodes near each voxel—where the averages were weighted to reflect patients who had more electrodes implanted near that location. This yielded a single map for each dataset, highlighting regions that are potentially promising implantation targets in terms of providing full-brain activity information via SuperEEG (Fig. 5A, B). Despite task and patient differences across the two datasets, we nonetheless found that the maps of the most promising implantation targets derived from both datasets were similar (voxelwise correlation between information scores across the two datasets: $r = 0.03, p < 10^{-10}$). While the correspondence between the two maps was not perfect, our finding that there were some commonalities between the two maps lends support to the notion that different brain areas are differently informative about full-brain activity patterns. Further, we found the intersection of the top 10% of the most informative voxels between the two datasets (Fig. S5) and found gray matter regions like the right postcentral gyrus, right supramarginal gyrus, and the right nucleus accumbens that exhibited strong information scores in both datasets may be especially promising implantation

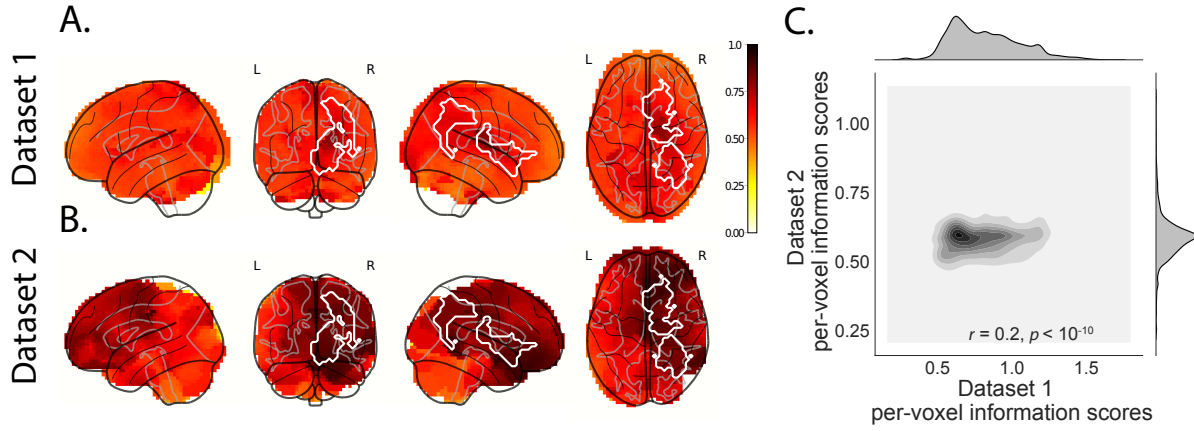


Figure 5: Most informative electrode locations. **A. Dataset 1 information score by voxel.** The voxel colors reflect the weighted average reconstruction accuracy across all electrodes from any patients with at least one electrode within 20 MNI units of the given voxel. **B. Dataset 2 information score by voxel.** This panel is in the same format as Panel A. In both panels the contours indicate the intersections between the top 10% most informative voxels in each map. **C. Correspondence in information scores by voxel across Datasets 1 and 2.** Same format as Figure 4C.

306 targets.

307 Discussion

308 Are our brain's networks static or dynamic? And to what extent are the network properties
 309 of our brains stable across people and tasks? One body of work suggests that our brain's
 310 *functional* networks are dynamic [e.g., ?], person-specific [e.g., ?], and task-specific [e.g.,
 311 ?]. In contrast, although the gross anatomical structure of our brains changes meaningfully
 312 over the course of years as our brains develop, on the timescales of typical neuroimaging ex-
 313 periments (i.e., hours to days) our anatomical networks are largely stable [e.g., ?]. Further,
 314 many aspects of brain anatomy, including white matter structure, are largely preserved across
 315 people [e.g., ? ? ?]. There are several possible means of reconciling this apparent inconsis-
 316 tency between dynamic person- and task-specific functional networks versus stable anatomical
 317 networks. For example, relatively small magnitude anatomical differences across people may

318 be reflected in reliable functional connectivity differences. Along these lines, one recent study
319 found that diffusion tensor imaging (DTI) structural data is similar across people, but may
320 be used to predict person-specific resting state functional connectivity data [?]. Similarly,
321 other work indicates that task-specific functional connectivity may be predicted by resting state
322 functional connectivity data [? ?]. Another (potentially complementary) possibility is that our
323 functional networks are constrained by anatomy, but nevertheless exhibit (potentially rapid)
324 task-dependent changes [e.g., ?].

325 Here we have taken a model-based approach to studying whether high spatiotemporal
326 resolution activity patterns throughout the human brain may be explained by a static connec-
327 tome model that is shared across people and tasks. Specifically, we trained a model to take
328 in recordings from a subset of brain locations, and then predicted activity patterns during the
329 same interval, but at *other* locations that were held out from the model. Our model, based on
330 Gaussian process regression, was built on three general hypotheses about the nature of the
331 correlational structure of neural activity (each of which we tested). First, we hypothesized that
332 functional correlations are stable over time and across tasks. We found that, although aspects
333 of the patients' functional correlations that were stable across tasks, we achieved better recon-
334 struction accuracy when we trained the model on within-task data [we acknowledge that our
335 general approach could potentially be extended to better model across-task changes, following
336 ? ? , and others]. Second, we hypothesized that some of the correlational structure of peo-
337 ple's brain activity is similar across individuals. Consistent with this hypothesis, our model
338 explained the data best when we trained the correlation model using data from *other* patients—
339 even when compared to a correlation model trained on the same patient's data. Third, we
340 resolved ambiguities in the data by hypothesizing that neural activity from nearby sources will
341 tend to be similar, all else being equal. This hypothesis was supported through our finding that
342 all of the models we trained that incorporated this spatial smoothness assumption predicted

343 held-out data well above chance.

344 One potential limitation of our approach is that it does not provide a natural means of
345 estimating the precise timing of single-neuron action potentials. Prior work has shown that
346 gamma band and broadband activity in the LFP may be used to estimate the firing rates of
347 neurons that underly the population contributing to the LFP [? ? ? ?]. Because SuperEEG
348 reconstructs LFPs throughout the brain, one could in principle use gamma or broadband power
349 in the reconstructed signals to estimate the corresponding firing rates (though not the timings
350 of individual action potentials).

351 Beyond providing a means of estimating ongoing activity throughout the brain using al-
352 ready implanted electrodes, our work also has implications for where to place the electrodes in
353 the first place. Electrodes are typically implanted to maximize coverage of suspected epilep-
354 togenic tissue. However, our findings suggest that this approach could be further optimized.
355 Specifically, one could leverage not only the non-invasive recordings taken during an initial
356 monitoring period (as is currently done routinely), but also recordings collected from other
357 patients. We could then ask: given what we learn from other patients' data (and potentially
358 from the scalp EEG recordings of this new patient), where should we place a fixed number of
359 electrodes to maximize our ability to map seizure foci? As shown in Figure 5, recordings from
360 different locations are differently informative in terms of reconstructing the spatiotemporal
361 activity patterns throughout the brain. This property might be leveraged in decisions about
362 where to surgically implant electrodes in future patients.

363 **Concluding remarks**

364 Over the past several decades, neuroscientists have begun to leverage the strikingly profound
365 mathematical structure underlying the brain's complexity to infer how our brains carry out
366 computations to support our thoughts, actions, and physiological processes. Whereas tradi-

367 tional beamforming techniques rely on geometric source-localization of signals measured at the
368 scalp, here we propose an alternative approach that leverages the rich correlational structure
369 of two large datasets of human intracranial recordings. In doing so, we are one step closer to
370 observing, and perhaps someday understanding, the full spatiotemporal structure of human
371 neural activity.

372 **Code availability**

373 We have published an open-source toolbox implementing the SuperEEG algorithm. It may
374 be downloaded [here](#). Additionally, we have provided notebooks for all analyses and figures
375 reported here.

376 **Data availability**

377 The dataset analyzed in this study was generously shared by Michael Kahana. A portion of
378 Dataset 1 may be downloaded [here](#). Dataset 2 may be downloaded [here](#).

379 **Acknowledgements**

380 We are grateful for useful discussions with Luke J. Chang, Uri Hasson, Josh Jacobs, Michael
381 Kahana, and Matthijs van der Meer. We are also grateful to Michael Kahana for generously
382 sharing the ECoG data we analyzed in our paper, which was collected under NIMH grant
383 MH55687 and DARPA RAM Cooperative Agreement N66001-14-2-4-032, both to MJK. Our
384 work was also supported in part by NSF EPSCoR Award Number 1632738 and by a sub-
385 award of DARPA RAM Cooperative Agreement N66001-14-2-4-032 to JRM. The content is solely
386 the responsibility of the authors and does not necessarily represent the official views of our
387 supporting organizations.

388 **Author Contributions**

389 J.R.M conceived and initiated the project. L.L.W.O. and A.C.H. performed the analyses. J.R.M.
390 and L.L.W.O. wrote the manuscript.

391 **Author Information**

392 Reprints and permissions information is available at www.nature.com/reprints. The authors
393 declare no competing financial interests. Readers are welcome to comment on the online
394 version of the paper. Publisher's note: Springer Nature remains neutral with regard to jurisdic-
395 tional claims in published maps and institutional affiliations. Correspondence and requests for
396 materials should be addressed to J.R.M. (jeremy.r.manning@dartmouth.edu).

397 **References**

- 398 [] Baillet, S., Mosher, J. C., and Leahy, R. M. (2001). Electromagnetic brain mapping. *IEEE Signal
399 Processing Magazine*, 18:14–30.
- 400 [] Becker, C. O., Pequito, S., Pappas, G. J., Miller, M. B., adn D S Bassett, S. T. G., and Preciado,
401 V. M. (2018). Spectral mapping of brain functional connectivity from diffusion imaging.
402 *Scientific Reports*, 8(1411):<https://doi.org/10.1038/s41598-017-18769-x>.
- 403 [] Betzel, R. F., Medaglia, J. D., Kahn, A. E., Soffer, J., Schonhaut, D. R., and Bassett, D. S.
404 (2017). Inter-regional ecog correlations predicted by communication dynamics, geometry,
405 and correlated gene expression. *arXiv*, page 1706.06088.
- 406 [] Casey, B. J., Giedd, J. N., and Thomas, K. M. (2000). Structural and functional brain develop-
407 ment and its relation to cognitive development. *Biological Psychology*, 54(1–3):241–257.
- 408 [] Cole, M. W., Ito, T., Bassett, D. S., and Schultz, D. H. (2016). Activity flow over resting-state
409 networks shapes cognitive task activations. *Nature Neuroscience*, 19(12):1718–1726.

- 410 [] Crone, N. E., Korzeniewska, A., and Franaszczuk, P. (2011). Cortical gamma responses:
411 searching high and low. *International Journal of Psychophysiology*, 79(1):9–15.
- 412 [] Ezzyat, Y., Kragel, J. E., Burke, J. F., Levy, D. F., Lyalenko, A., Wanda, P., O’Sullivan, L.,
413 Hurley, K. B., Busygin, S., Pedisich, I., Sperling, M. R., Worrell, G. A., Kucewicz, M. T., Davis,
414 K. A., Lucas, T. H., Inman, C. S., Lega, B. C., Jobst, B. C., Sheth, S. A., Zaghloul, K., Jutras,
415 M. J., Stein, J. M., Das, S. R., Gorniak, R., Rizzuto, D. S., and Kahana, M. J. (2017). Direct
416 brain stimulation modulates encoding states and memory performance in humans. *Current
Biology*, 27:1–8.
- 417
- 418 [] Ezzyat, Y., Wanda, P. A., Levy, D. F., Kadel, A., Aka, A., Pedisich, I., Sperling, M. R.,
419 Sharan, A. D., Lega, B. C., Burks, A., Gross, R. E., Inman, C. S., Jobst, B. C., Goren-
420 stein, M. A., Davis, K. A., Worrell, G. A., Kucewicz, M. T., Stein, J. M., Gorniak, R.,
421 Das, S. R., Rizzuto, D. S., and Kahana, M. J. (2018). Closed-loop stimulation of tem-
422 poral cortex rescues functional networks and improves memory. *Nature Communications*,
423 9(365):<https://doi.org/10.1038/s41467-017-02753-0>.
- 424 [] Finn, E. S., Shen, X., Scheinost, D., Rosenberg, M. D., Huang, J., Chun, M. M., Papademetris,
425 X., and Constable, R. T. (2015). Functional connectome fingerprinting: identifying individuals
426 using patterns of brain connectivity. *Nature Neuroscience*, 18:1664 – 1671.
- 427 [] Grabner, G., Janke, A. L., Budge, M. M., Smith, D., Pruessner, J., and Collins, D. L. (2006).
428 Symmetric atlasing and model based segmentation: an application to the hippocampus in
429 older adults. *Medical Image Computing and Computer-Assistend Intervention*, 9:58–66.
- 430 [] Hillebrand, A., Singh, K. D., Holliday, I. E., Furlong, P. L., and Barnes, G. R. (2005). A new
431 approach to neuroimaging with magnetoencephalography. *Human Brain Mapping*, 25:199–
432 211.

- 433 [] Horak, P. C., Meisenhelter, S., Song, Y., Testorf, M. E., Kahana, M. J., Viles, W. D., Bujarski,
434 K. A., Connolly, A. C., Robbins, A. A., Sperling, M. R., Sharan, A. D., Worrell, G. A., Miller,
435 L. R., Gross, R. E., Davis, K. A., Roberts, D. W., Lega, B., Sheth, S. A., Zaghloul, K. A., Stein,
436 J. M., Das, S. R., Rizzuto, D. S., and Jobst, B. C. (2017). Interictal epileptiform discharges
437 impair word recall in multiple brain areas. *Epilepsia*, 58(3):373–380.
- 438 [] Huster, R. J., Debener, S., Eichele, T., and Herrmann, C. S. (2012). Methods for simultaneous
439 EEG-fMRI: an introductory review. *The Journal of Neuroscience*, 32(18):6053–6060.
- 440 [] Jacobs, J., Kahana, M. J., Ekstrom, A. D., Mollison, M. V., and Fried, I. (2010). A sense of
441 direction in human entorhinal cortex. *Proceedings of the National Academy of Sciences, USA*,
442 107(14):6487–6482.
- 443 [] Jahanshad, N., Kochunov, P. V., Sprooten, E., Mandl, R. C., Nichols, T. E., Almasy, L., Blangero,
444 J., Brouwer, R. M., Curran, J. E., de Zubicaray, G. I., Duggirala, R., Fox, P. T., Hong, L. E.,
445 Landman, B. A., Martin, N. G., McMahon, K. L., Medland, S. E., Mitchell, B. D., Olvera, R. L.,
446 Peterson, C. P., Starr, J. M., Sussmann, J. E., Toga, A. W., Wardlaw, J. M., Wright, M. J., Pol, H.
447 E. H., Pastin, M. E., McIntosh, A. M., Deary, I. J., Thompson, P. M., and Glahn, D. C. (2013).
448 Multi-site genetic analysis of diffusion images and voxelwise heritability analysis: A pilot
449 project of the enigma-dti working group. *NeuroImage*, 81(1):455–469.
- 450 [] Kragel, J. E., Ezzyat, Y., Sperling, M. R., Gorniak, R., Worrell, G. A., Berry, B. M., Inman, C.,
451 Lin, J.-J., Davis, K. A., Das, S. R., Stein, J. M., Jobst, B. C., Zaghloul, K. A., Sheth, S. A., Rizzuto,
452 D. S., and Kahana, M. J. (2017). Similar patterns of neural activity predict memory formation
453 during encoding and retrieval. *NeuroImage*, 155:70–71.
- 454 [] Kucewicz, M. T., Berry, B. M., Kremen, V., Brinkmann, B. H., Sperling, M. R., Jobst, B. C.,
455 Gross, R. E., Lega, B., Sheth, S. A., Stein, J. M., Das, S. R., Gorniak, R., Stead, S. M., Rizzuto,

- 456 D. S., Kahana, M. J., and Worrell, G. A. (2017). Dissecting gamma frequency actiivty during
457 human memory processing. *Brain*, 140:1337–1350.
- 458 [] Kucewicz, M. T., Berry, B. M., Miller, L. R., Khadjevand, F., Ezzyat, Y., Stein, J. M., Kremen,
459 V., Brinkmann, B. H., Wanda, P., Sperling, M. R., Gorniak, R., Davis, K. A., Jobst, B. C., Gross,
460 R. E., Lega, B., Gompel, J. V., Stead, S. M., Rizzuto, D. S., Kahana, M. J., and Worrell, G. A.
461 (2018). Evidence for verbal memory enhancement with electrical brain stimulation in the
462 lateral temporal cortex. *Brain*, 141(4):971–978.
- 463 [] Lin, J.-J., Rugg, M. D., Das, S., Stein, J., Rizzuto, D. S., Kahana, M. J., and Lega, B. C.
464 (2017). Theta band power increases in the posterior hippocampus predict successful episodic
465 memory encoding in humans. *Hippocampus*, 27:1040–1053.
- 466 [] Manning, J. R., Jacobs, J., Fried, I., and Kahana, M. J. (2009). Broadband shifts in LFP power
467 spectra are correlated with single-neuron spiking in humans. *The Journal of Neuroscience*,
468 29(43):13613–13620.
- 469 [] Manning, J. R., Polyn, S. M., Baltuch, G., Litt, B., and Kahana, M. J. (2011). Oscillatory
470 patterns in temporal lobe reveal context reinstatement during memory search. *Proceedings of
471 the National Academy of Sciences, USA*, 108(31):12893–12897.
- 472 [] Manning, J. R., Ranganath, R., Norman, K. A., and Blei, D. M. (2014). Topographic fac-
473 tor analysis: a Bayesian model for inferring brain networks from neural data. *PLoS One*,
474 9(5):e94914.
- 475 [] Manning, J. R., Sperling, M. R., Sharan, A., Rosenberg, E. A., and Kahana, M. J. (2012).
476 Spontaneously reactivated patterns in frontal and temporal lobe predict semantic clustering
477 during memory search. *The Journal of Neuroscience*, 32(26):8871–8878.

- 478 [] Manning, J. R., Zhu, X., Willke, T. L., Ranganath, R., Stachenfeld, K., Hasson, U., Blei,
479 D. M., and Norman, K. A. (2018). A probabilistic approach to discovering dynamic full-brain
480 functional connectivity patterns. *NeuroImage*.
- 481 [] Miller, K. J., Shenoy, P., den Nijs, M., Sorensen, L. B., Rao, R. P. N., and Ojemann, J. G. (2008).
482 Beyond the gamma band: the role of high-frequency features in movement classification.
483 *IEEE Transactions on Biomedical Engineering*, 55(5):1634 – 1637.
- 484 [] Mori, S., Oishi, K., Jiang, H., Jiang, L., Li, X., Akhter, K., Hua, K., Faria, A. V., Mahmood, A.,
485 Woods, R., Toga, A. W., Pike, G. B., Neto, P. R., Evans, A., Zhang, J., Huang, H., Miller, M. I.,
486 van Zijl, P., and Mazziotta, J. (2008). Stereotaxic white matter atlas based on diffusion tensor
487 imaging in an icbm template. *NeuroImage*, 40(2):570–582.
- 488 [] Rasmussen, C. E. (2006). *Gaussian processes for machine learning*. MIT Press.
- 489 [] Sarvas, J. (1987). Basic mathematical and electromagnetic concepts of the biomagnetic inverse
490 problem. *Phys. Med. Biol.*, 32(1):11–22.
- 491 [] Sawyer, R. J. (1995). *The Terminal Experiment*. HarperPrism.
- 492 [] Sederberg, P. B., Kahana, M. J., Howard, M. W., Donner, E. J., and Madsen, J. R. (2003). Theta
493 and gamma oscillations during encoding predict subsequent recall. *Journal of Neuroscience*,
494 23(34):10809–10814.
- 495 [] Sederberg, P. B., Schulze-Bonhage, A., Madsen, J. R., Bromfield, E. B., Litt, B., Brandt, A., and
496 Kahana, M. J. (2007a). Gamma oscillations distinguish true from false memories. *Psychological
497 Science*, 18(11):927–932.
- 498 [] Sederberg, P. B., Schulze-Bonhage, A., Madsen, J. R., Bromfield, E. B., McCarthy, D. C.,
499 Brandt, A., Tully, M. S., and Kahana, M. J. (2007b). Hippocampal and neocortical gamma
500 oscillations predict memory formation in humans. *Cerebral Cortex*, 17(5):1190–1196.

- 501 [] Sejnowski, T. J., Churchland, P. S., and Movshon, J. A. (2014). Putting big data to good use in
502 neuroscience. *Nature Neuroscience*, 17:1440–1441.
- 503 [] Snyder, A. Z. (1991). Dipole source localization in the study of EP generators: a critique.
504 *Electroencephalography and Clinical Neurophysiology*, 80(4):321–325.
- 505 [] Solomon, E. A., Gross, R., Lega, B., Sperling, M. R., Worrell, G., Sheth, S. A., Zaghloul, K. A.,
506 Jobst, B. C., Stein, J. M., Das, S., Gorniak, R., Inman, C., Seger, S., Kragel, J. E., Rizzuto, D. S.,
507 and Kahana, M. J. (2018). Mtl functional connectivity predicts stimulation-induced theta
508 power. *Nature Communications*, In press.
- 509 [] Sporns, O. and Betzel, R. F. (2016). Modular brain networks. *Annual Review of Psychology*,
510 67:613–640.
- 511 [] Talairach, J. and Tournoux, P. (1988). *Co-planar stereotaxic atlas of the human brain*. Verlag,
512 Stuttgart.
- 513 [] Tavor, I., Jones, O. P., Mars, R. B., Smith, S. M., Behrens, T. E., and Jbabdi, S. (2016). Task-
514 free MRI predicts individual differences in brain activity during task performance. *Science*,
515 352(6282):216–220.
- 516 [] Turk-Browne, N. B. (2013). Functional interactions as big data in the human brain. *Science*,
517 342:580–584.
- 518 [] Weidemann, C. T., Kragel, J. E., Lega, B. C., Worrell, G. A., Sperling, M. R., Sharan, A. D.,
519 Jobst, B. C., Khadjevand, F., Davis, K. A., Wanda, P. A., Kadel, A., Rizzuto, D. S., and Kahana,
520 M. J. (2018). Neural activity reveals interactions between episodic and semantic memory
521 systems during retrieval. *Journal of Experimental Psychology: General*, In press.
- 522 [] Yeo, B. T. T., Krienen, F. M., Sepulcre, J., Sabuncu, M. R., Lashkari, D., Hollinshead, M.,
523 Roffman, J. L., Smoller, J. W., Zollei, L., Polimieni, J. R., Fischl, B., Liu, H., and Buckner,

- 524 R. L. (2011). The organization of the human cerebral cortex estimated by intrinsic functional
525 connectivity. *Journal of Neurophysiology*, 106(3):1125–1165.